Journal of Catalysis 282 (2011) 1–12

Contents lists available at ScienceDirect

Journal of Catalysis

journal homepage: www.elsevier.com/locate/jcat

Easy synthesis of three-dimensionally ordered macroporous $La_{1-x}K_xCoO_3$ catalysts and their high activities for the catalytic combustion of soot

Junfeng Xu, Jian Liu, Zhen Zhao *, Chunming Xu, Jianxiong Zheng, Aijun Duan, Guiyuan Jiang

State Key Laboratory of Heavy Oil, China University of Petroleum, Beijing 102249, People's Republic of China

ARTICLE INFO

Article history:
Received 23 January 2011
Revised 4 March 2011
Accepted 26 March 2011
Available online 12 July 2011

Keywords:
Synthesis
$La_{1-x}K_xCoO_3$ catalysts
Catalytic combustion
Soot
Three-dimensionally ordered macroporous oxides
Carboxy-modified colloidal crystal templating method

ABSTRACT

Three-dimensionally ordered macroporous (3DOM) $La_{1-x}K_xCoO_3$ ($x = 0$–0.3) perovskite-type oxide catalysts with large pore sizes and interconnected macroporous frameworks were successfully synthesized by a novel method of carboxy-modified colloidal crystal templates (CMCCT). The obtained catalysts were characterized by means of XRD, FT-IR, SEM, TEM, BET, XPS, and H_2 TPR. The detailed preparation process was investigated using in situ TG–DSC, Raman, and EDS analyses. The sp^2-hybridized carbon atoms of the modified polymer templates can be converted to sturdy amorphous carbon materials by calcination under an inert atmosphere to prevent the macrostructure from collapsing. The active site densities of catalysts were determined by isothermal anaerobic titration, and their turnover frequency (TOF) values were then calculated. The catalytic performances for soot combustion were evaluated using temperature-programmed oxidation (TPO) reaction technology. 3DOM $La_{1-x}K_xCoO_3$ catalysts exhibited catalytic activities as high as that of noble metal Pt catalysts under loose contact conditions.

1. Introduction

The emission control of diesel soot, which is causing severe environmental and health problems, has become one of the focal research topics in the field of environmental catalysis. Since the reduction in soot particulate emissions cannot be accomplished by engine modifications alone, catalytic processes need to be developed [1]. For catalytic oxidation of diesel soot, there are two challenges to enhance catalytic performance: designing appropriate catalytic materials that possess strong redox ability, and designing new systems of catalysts that improve the contact between the soot and the catalyst.

Several kinds of catalysts, which have excellent redox abilities, have exhibited high catalytic activities for soot combustion, such as precious metals [2], transition metal oxides [3,4], alkaline metal oxides [5], perovskite or perovskite-like oxides [6–8], and ceria-based oxides [9–11]. However, these conventional catalysts have the limitation that their pore sizes (<10 nm) are much smaller than those of soot particles (>25 nm [12]). The soot cannot touch the active sites on the internal surfaces of catalysts; only those on external surfaces of catalysts are available for soot combustion. Thus, the efficiency of catalysts is strongly influenced by the contact between the soot and the catalyst. The unique advantages of three-dimensionally ordered macroporous (3DOM) materials for diesel soot combustion have been discovered in recent years [13,14]. Their large pore sizes (>50 nm) and interconnected macroporous tunnels not only could permit soot particles to enter their inner pores, where the catalytic combustion of soot could proceed, but also could allow the soot particles to transfer easily through the structure and to have less diffusion resistance to reaching active sites. Thus, the contact between the soot and the catalyst will be improved remarkably, and the catalytic activity of the catalyst will be enhanced dramatically [15].

So far, various kinds of 3DOM single metal oxides have been prepared by the colloidal crystal templating (CCT) method [16] through alkoxide-based sol–gel processes. But this method becomes difficult for the formation of 3DOM complex metal oxides, because of the difficulty and high cost of obtaining metal alkoxide precursors [17]. Moreover, these metal salts will melt at a temperature lower than that for the decomposition of the polymer templates, which will destroy the 3DOM structure. Yan et al. [18] prepared 3DOM metal oxides (MgO, Cr_2O_3, MnO_2, Fe_2O_3) using other metal salts (acetate or nitrate) as precursors, which does not require any metal alkoxides. The metal salts are converted to metal oxalates by reacting with oxalic acid, and then converted to metal oxides before the decomposition of polymer templates. However, this method is not suitable for the preparation of 3DOM perovskite-type complex metal oxides, because different metals have different reactivities with oxalic acid or base, and the produced oxalate salts or metal hydroxides have different

---

* Corresponding author. Fax: +86 10 69724721.
E-mail address: zhenzhao@cup.edu.cn (Z. Zhao).

0021-9517/$ - see front matter © 2011 Elsevier Inc. All rights reserved.
doi:10.1016/j.jcat.2011.03.024

solubilities in the reacting media, which will result in obtained complex metal oxides with undesired metal ratios. Recently, an elegant method for successfully producing the 3DOM perovskite-type complex metal oxides, $LaFeO_3$, $LaMnO_3$, and $LaCrO_3$, was developed by Sadakane et al. [13]. This method, using ethylene glycol as a complexing agent, consists of the low-temperature oxidation of ethylene glycol to the glyoxylate dianion by a metal nitrate; the metal glyoxylates can be converted to their metal oxides at relatively low temperatures. Unfortunately, the Co-based perovskite-type complex metal oxides with 3DOM structure cannot be obtained using this method, although $LaCoO_3$ catalyst has the highest catalytic activity among various perovskite-type oxides for soot combustion, according to the results reported by Hong and Lee [19].

To obtain the 3DOM structure, two requirements should be satisfied in the polymer CCT method. First, the metal precursor should be transformed to a solid state framework before the polymer templates melt. Second, the solid state material should be converted to the desired metal oxides before the polymer templates decompose. Therefore, a theory of the preparation of 3DOM complex metal oxides by the polymer CCT method was proposed in which the solidification temperature (T_s) for the metal precursor converting to a solid state framework should be lower than the glass transition temperature (T_g) of polymer templates [13], and the formation temperature (T_f) of the desired metal oxides should be lower than the decomposition temperature (T_d) of polymer templates. Otherwise, the macroporous framework will collapse during the calcination process. Both limitations lead to the hard preparation of some 3DOM perovskite-type complex metal oxides directly from the metals (Cu, Ni, Zn, Co, Mg, Ca, Ce) by the polymer CCT method [20].

In this paper, we first reported the easy synthesis of 3DOM $La_{1-x}K_xCoO_3$ ($x = 0–0.3$) perovskite-type complex metal oxides by the carboxy-modified colloidal crystal templating (CMCCT) method. The detailed preparation process was investigated by means of in situ TG–DSC, SEM, Raman spectroscopy, and EDS. The turnover frequency (TOF) values of catalysts were measured through the isothermal reaction method. The influences of K-substitution and the macroporous structures of catalysts on the catalytic performances in soot combustion were also discussed.

2. Experimental

2.1. Preparation

3DOM $La_{1-x}K_xCoO_3$ perovskite-type oxide catalysts were prepared by the CMCCT method. Stoichiometric amounts of metal nitrates ($La(NO_3)_3{\cdot}6H_2O$, $Co(NO_3)_2{\cdot}6H_2O$, KNO_3) were dissolved with ethylene glycol and methanol (40 vol%) under stirring at room temperature for 5 h. Then the mixed solution was added to the c-PMMA templates to permeate into the voids between the close-packed spheres. Excess solution was removed from the impregnated templates by filtration. The obtained precursor/template mixture was allowed to dry at room temperature in air overnight. Finally, the dried sample was mixed with quartz sand (10–15 mesh) and first calcined under Ar at 130 °C for 2 h in a tube furnace, then under temperature linearly rising at a rate of 1 °C/min to 700 °C and held for 5 h, and subsequently treated at 700 °C in air for 5 h. The flow rates of both Ar and air were 80 ml/min. The samples obtained by heat treatment under Ar, calcination in air, and both heat treatment under Ar and calcination in air are denoted as CMCCT-Ar, CMCCT-Air, and CMCCT-Ar-Air, respectively.

The nanoparticle $La_{1-x}K_xCoO_3$ perovskite-type oxide catalysts were prepared by the citric acid–ligated combustion method with various metal nitrates ($La(NO_3)_3{\cdot}6H_2O$, $Co(NO_3)_2{\cdot}6H_2O$, KNO_3) as precursors. The preparation method was described in literature [21].

2.2. Characterization

The crystal structures of the fresh catalysts were determined with a powder X-ray diffractometer (Shimadzu XRD 6000), using Cu Kα ($\lambda = 0.1542$ nm) radiation combined with a nickel filter operating at 40 kV and 10 mA. The diffractometer data were recorded for 2θ values from 5° to 90° at a scanning rate of 4°/min. The patterns were compared with JCPDS reference data for phase identification.

Fourier transform infrared spectroscopy (FT-IR) absorbance spectra were obtained at wavenumbers ranging from 6000 to 400 cm^{-1} via a FTS-3000 spectrophotometer manufactured by American Digilab. The measured wafer was prepared as a KBr pellet with a 1/100 weight ratio of sample to KBr. The resolution was set at 2 cm^{-1} during measurement.

The Brunauer–Emmett–Teller (BET) surface areas were measured by N_2 adsorption and desorption using a Micromeritics ASAP 2010 analyzer.

The scanning electron microscopy (SEM) images were observed, and energy-dispersive spectroscopy (EDS) results were obtained on an FEI Quanta 200F SEM. The internal morphology and grain characteristics were observed by transmission electron microscopy (TEM), using a JEO1 JEM 2100 electron microscope equipped with a field emission source at an accelerating voltage of 200 kV.

X-ray photoelectron spectroscopy (XPS) spectra were recorded using a Kratos XSAM800 spectrometer with a standard Al*K* source (1486.6 eV) working at 350 W. The working pressure was less than 2×10^{-7} Pa. The spectrometer was calibrated by assuming the binding energy (BE) of the $Au4f_{7/2}$ line to lie at 84.0 eV with respect to the Fermi level.

Raman spectra were obtained with a Jobin Yvon LabRam-HR spectrometer (HR800), using a semiconductor laser with excitation wavelength 532 nm.

Thermogravimetry–differential scanning calorimetry (TG–DSC) analyses were performed by a Rigaku TAS-300 thermobalance. Typically, a 50-mg sample was put into the sample holder inside an aluminum crucible, using an empty crucible in the reference holder. The sample was subjected to a linear rise of temperature from 100 to 700 °C with a heating rate of 10 °C/min under an air or Ar flow.

Temperature-programmed reduction with H_2 (H_2 TPR) measurements were performed in a conventional flow apparatus. A 30-mg sample was pretreated in air by calcination at 600°C for 1 h and subsequently cooled to 100°C. Afterward, a 10% H_2/He flow (40 ml/min) was passed over the catalyst bed while the temperature was ramped from 100 to 900°C at a heating rate of 10°C/min. The hydrogen consumption signal was monitored by a thermal conductivity detector (TCD). Before the outlet gases entered the TCD, a cooling trap and a filter packed with molecular sieve 5A (60–80 mesh) were used to remove H_2O and CO_2.

2.3. Catalytic activity measurement

2.3.1. The TPO reaction

The catalytic performance of the 3DOM $La_{1-x}K_xCoO_3$ perovskite-type oxide catalysts was evaluated with a temperature-programmed oxidation (TPO) reaction on a fixed-bed tubular quartz system. The reaction temperature was controlled through a PID regulation system based on measurements with a K-type thermocouple and varied during each TPO run from 200 to 600°C at a rate of 2°C/min. The model soot, Printex-U, used in this work was provided by Degussa. Its primary particle size was 25 nm and its specific surface was 100 m^2/g. The catalyst and soot were mixed at a mass ratio of 10:1 with a spatula to reproduce the loose contact mode, which is the most representative model of diesel soot particles flowing through a catalytic filter. Then the mixture was placed in the tubular quartz reactor (reactor diameter ϕ = 10 mm) in every test. The occurrence of heat and mass transfer limitations influenced the observed reaction rates. In addition, it was also found to affect soot combustion temperatures by about 0–5°C. In order to accurately detect the true reaction temperatures, the catalyst–soot fixed bed was sandwiched between two quartz-wool layers and the tip of a K-type thermocouple was located well inside the catalyst bed itself. Reactant gases containing 5% O_2 and 0.2% NO balanced with Ar were passed through a mixture of catalyst and soot at a flow rate of 50 ml/min. The outlet gas compositions coming from the reactor were analyzed with an online gas chromatograph (GC, Sp-3420, Beijing) using FID detectors. The FID was employed to determine CO and CO_2 concentrations after these gases were separated over a Porapak N column and converted to CH_4 over a Ni catalyst at 380 °C. The selectivity to CO_2 formation (S_{CO2}) was defined as the CO_2 outlet concentration (C_{CO2}) divided by the sum of the CO_2 and CO outlet concentrations; i.e., $S_{CO2} = C_{CO2}/(C_{CO} + C_{CO2})$. S^m_{CO2} was denoted as the S_{CO2} at the temperature at which the soot-burnt rate was the highest. The catalytic activity was evaluated by the values of T_{50}, which was defined as the temperature at which 50% of the soot was oxidized during the TPO procedure.

2.3.2. The isothermal reaction

The intrinsic activity of the catalyst was based on the TOF value, which was defined as the ratio of the reaction rate to the active site density of catalysts. The reaction rate of soot combustion was determined by an isothermal reaction at 320 °C in the kinetic regime; the influences of internal and external mass and heat transfer were all excluded. The total flow rate was 150 ml/min, and the reaction gas composition was the same as for the TPO reaction. The selection of 320 °C was made because the soot conversion was low (<10%) and nearly constant over time. The uniform macroporous structure and the small particle diameter (<40 μm) of catalysts could exclude the intraparticle mass transport limitations. For a total flow rate of 150 ml/min, no external mass transport limitations were detected [22,23]. The gas analyses were then used to calculate the reaction rate (v) and the specific reaction rate normalized by unit BET surface area (v^*) for soot combustion using the equation [24]

$$v = -\frac{dn}{m\,dt} = \frac{CO_2 \times Q_C}{m}; \quad v^* = \frac{v}{S} = \frac{CO_2 \times Q_C}{mS}$$

where CO_2 is the measured molar fraction of these species in the gas phase, Q_c is the molar flow rate of gases through the reactor (mol), m is the mass of the catalyst (g), and S is the BET surface area of the catalyst (m^2/g).

The active site density of catalysts was calculated by isothermal anaerobic titrations. During this process, the soot was regarded as the probe molecule. When the concentration of the produced CO_2 became stable, O_2 was instantaneously removed from the reactant stream. The transient decay in concentration from the steady state was monitored with an online gas chromatograph using an FID detector. Before experiments, the samples were carefully calibrated with standard gas. Moreover, to avoid the influence of the residual oxygen, the distance between the samples and the detector was as short as possible (about 1 m) and a relatively high feed flow rate (150 ml/min) was used. The number of active redox sites (O^* amount) and the density of active redox sites (O^* density) available to soot under these reaction conditions can be quantified by integrating the diminishing rate of CO_2 formation over time [22],

$$O^* \text{ amount (mol/g)} = \frac{2P_0V \times A \times 10^{-6}}{RTm}, \tag{1}$$

$$O^* \text{ density } (\text{nm}^{-2}) = \frac{O^* \text{ amount}}{S \times 10^{18}} \times 6.02 \times 10^{23}, \tag{2}$$

where A is the integrated area of the CO_2 concentration as a function of time (s), V is the volumetric flow rate of gases through the reactor (m^3/s), m is the mass of the catalyst (g), P_0 is the atmospheric pressure (Pa), R is the gas constant, T is the room temperature (K), and S is the BET surface area of the catalyst (m^2/g).

3. Results

3.1. Preparation and characterization of the catalysts

3.1.1. The preparation of catalysts

Scheme 1 shows the preparation of 3DOM complex metal oxides by the CMCCT method. The c-PMMA spheres were synthesized using the modified emulsifier-free emulsion polymerization technique and then were assembled to a three-dimensionally ordered arrangement as colloidal crystal templates. After drying in air, the templates were impregnated by the precursor solution. Finally, the precursor/template mixtures were calcined under Ar and in air, respectively. When calcined under Ar, the sp^2-hybridized carbon atoms could be converted to sturdy amorphous carbon materials that could be used as hard templates to prevent the macrostructure of the catalysts from collapsing, and the carbon templates could be removed by heat treatment in air. The detailed preparation process is described in the Supplementary Information.

Fig. 1a and b show SEM and TEM images of the 3DOM $LaCoO_3$ catalyst obtained by the CMCCT method, respectively. The images indicate that the obtained 3DOM catalyst contains an interconnected macroporous framework. The next layer of the macroporous structure is clearly visible in the enlarged SEM image (inset in Fig. 1a) and the voids are interconnected through open windows, ca. 100 nm in diameter. The wall is crystallized, which is confirmed by selected area electron diffraction (SAED) (inset in Fig. 1b). In addition, SEM images of the samples calcined under different conditions are also shown in Fig. 1c and d. According to the SEM image of CMCCT-Ar in Fig. 1c, the 3DOM structure can be retained by the carbon templates even when the calcination temperature reaches 700 °C. In contrast, the macroporous structure of CMCCT-Air collapsed, as shown in Fig. 1d. This may be due to the absence of hard carbon templates to support the macroporous framework at high temperature while the polymer templates decompose.

3.1.2. The results of XRD characterization

The XRD patterns of 3DOM $La_{1-x}K_xCoO_3$ catalysts are shown in Fig. 2a. The diffraction peaks of catalysts are in good agreement with the standard file (JCPDS25–1060). The characteristic diffraction peaks with 2θ values at 23.3°, 32.9°, 40.7°, 47.5°, 58.7°, 69.0°, and 78.8° correspond to (012), (110), (202), (024), (300), (220), and (134) lattice faces of rhombohedral perovskite-type $LaCoO_3$, respectively. This indicates the formation of perovskite-type structure in the 3DOM catalysts. Very weak peaks at a 2θ value of 37° appear when the K-substituted amounts are greater than 0.1. This may be because a small amount of Co_3O_4 was formed when La^{3+} ions were partially replaced by K^+ ions. Furthermore, the (110) diffraction peak shifts to higher angle with the increasing K-substituted amount as shown in Fig. 2b, indicating that the K^+ ions are incorporated into the perovskite-type structure of catalysts. The average crystallite sizes (D) of all catalysts were estimated by the Debye–Scherrer equation using the XRD data of the most prominent line: $D\ (hkl) = 0.89\lambda/(\beta \cos \theta)$, where β is the half-height width of the diffraction peak of the catalyst, θ is the diffraction angle, and λ is the X-ray wavelength corresponding to the Cu$K\alpha$ radiation. The lattice parameters of catalysts were calculated by a standard cubic indexing method using the intensity of the most prominent peak, (110). As listed in Table 1, the average crystallite size of the 3DOM $LaCoO_3$ determined by the Scherrer

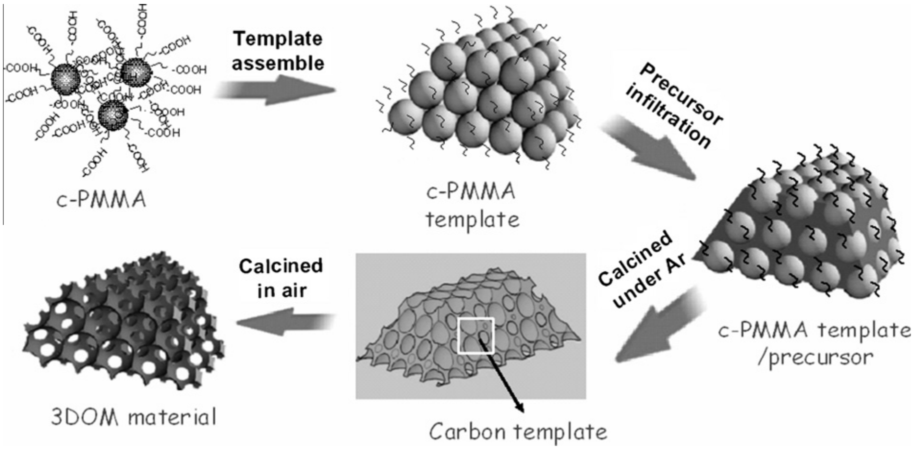

Scheme 1. Schematic illustration of the preparation of 3DOM catalysts.

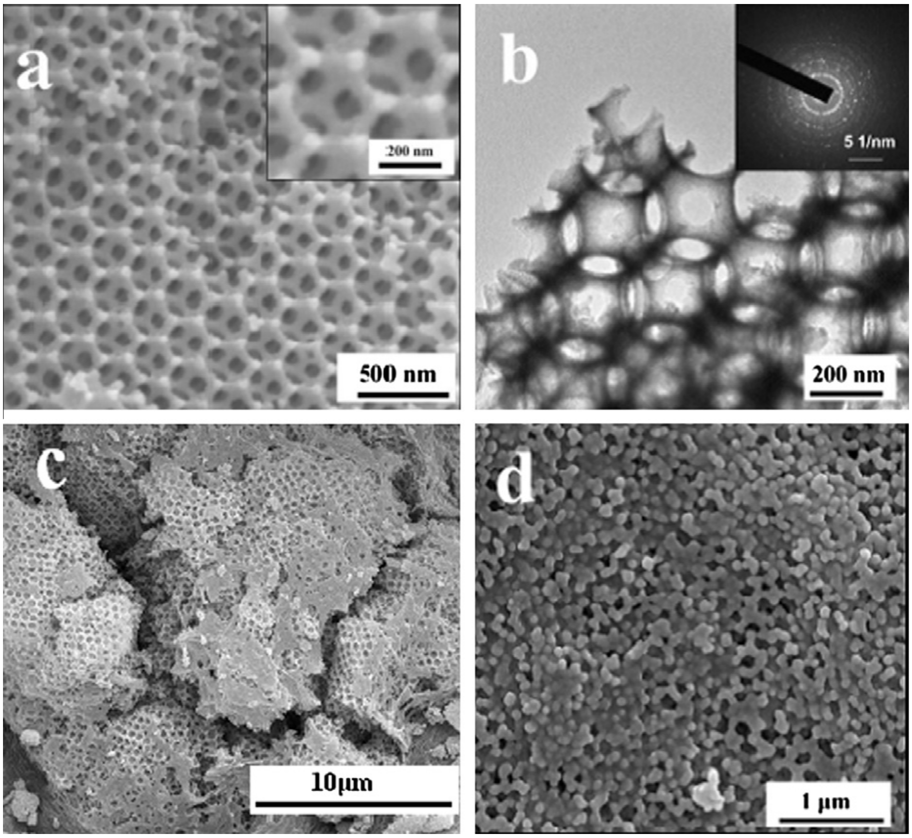

Fig. 1. The SEM and TEM images of the samples. (a) The SEM image of 3DOM $LaCoO_3$. Inset: The enlarged area of 3DOM $LaCoO_3$. (b) The TEM imageof 3DOM $LaCoO_3$. Inset: The SAED pattern of 3DOM $LaCoO_3$. (c) The SEM image of CMCCT-Ar. (d) The SEM image of CMCCT-Air.

equation is 17.9 nm, and with respect to the 3DOM $La_{1-x}K_xCoO_3$ catalysts, no obvious changes in their crystallite sizes are observed. Therefore, due to the relatively similar Goldschmidt ionic radii of La^{3+} (0.122 nm) and K^+ (0.133 nm), it can be concluded that substitution of K^+ ion into the A-site of 3DOM $LaCoO_3$ does not cause great impact on the crystalline phase, crystalline size, and crystallinity of the catalyst.

3.1.3. The results of FT-IR characterization

Fig. 3 shows the FT-IR spectra of the 3DOM $La_{1-x}K_xCoO_3$ catalysts. Three vibration bands at 596 cm^{-1} (very strong), 560 cm^{-1} (shoulder), and 425 cm^{-1} (strong) are observed in the spectra of all the catalysts. These bands are in agreement with the two normal modes of vibrational frequencies of perovskite-type structure reported by Couzi and Huong [25]. The vibration bands at 560 and 596 cm^{-1} can be assigned to two kinds of Co–O stretching vibrations in the BO_6 octahedron (ν_1), while 425 cm^{-1} belongs to the bending vibration of the Co–O bond (ν_2) [26]. Moreover, the vibration band at 596 cm^{-1} becomes broader and upshifts with the increase in the K-substituted amount. This may be due to the presence of high-valent Co ions, i.e., Co^{4+}, when K^+ ions partially replace La^{3+} ions, because the interaction and the wavenumber of the stretching vibration for Co^{4+}–O bonding are greater than those for Co^{3+}–O. In addition, new weak vibration bands at 667 cm^{-1}, which

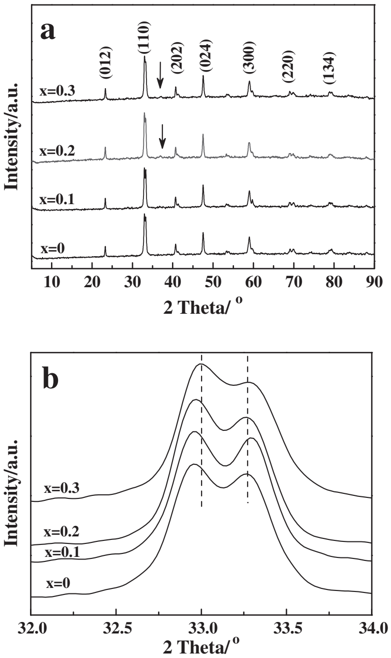

Fig. 2. The XRD patterns of 3DOM $La_{1-x}K_xCoO_3$ catalysts: (a) the whole range and (b) the enlarged small range ($2\theta = 32°–34°$).

Table 1
Average crystal parameters, crystal sizes, and BET surface areas of 3DOM $La_{1-x}K_xCoO_3$ catalysts.

Catalysts	Crystal face	I/I1	2θ (°)	D (nm)	BET (m^2/g)
$LaCoO_3$	110	100	32.91	17.9	29.5
$La_{0.9}K_{0.1}CoO_3$	110	100	33.39	17.0	27.4
$La_{0.8}K_{0.2}CoO_3$	110	100	33.08	17.3	22.7
$La_{0.7}K_{0.3}CoO_3$	110	100	33.06	17.1	20.8

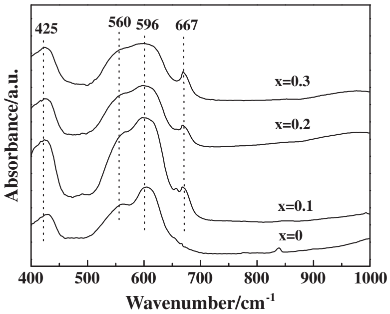

Fig. 3. The FT-IR spectra of 3DOM $La_{1-x}K_xCoO_3$ catalysts.

can be assigned to Co_3O_4, appear in the K-substituted catalysts and the intensity gradually increases with the increase in the K-substituted amount. This result also indicates the presence of Co_3O_4 when La^{3+} ions are partially replaced by K^+ ions, which is consistent with the XRD results.

3.1.4. The results of BET characterization

The BET surface areas of the 3DOM $La_{1-x}K_xCoO_3$ catalysts are listed in Table 1. All the 3DOM catalysts have relatively large surface areas, even calcined at 700 °C, which may be due to their uniform macroporous structures. The surface area of 3DOM $LaCoO_3$ is 29.5 m^2/g, which is about three times as much as for nanoparticle $LaCoO_3$ (9.0 m^2/g [21]). The large surface area of 3DOM catalysts can further increase the number of active sites of catalysts exposed to soot particles. Thus, they will exhibit superior catalytic activities compared with the nanoparticle ones. In addition, the BET surface area of 3DOM $La_{1-x}K_xCoO_3$ catalysts decreases with the increase in the K-substituted amount. This may be due to the formation of low-melting compounds or eutectics with other components of the catalysts that influence the ordered degree of the macrostructure of catalysts during the heat treatment.

3.1.5. The results of SEM characterization

Fig. 4 shows the SEM images of 3DOM $La_{1-x}K_xCoO_3$ catalysts. All the catalysts obtained by the CMCCT method consist of a skeleton surrounding uniform close-packed macropores. The macropores are interconnected through the windows, which are formed because no precursor solution is present in the contact areas among the polymer spheres. The average diameters of their pores are about 240–260 nm, which correspond to a shrinkage of ca. 20% compared with the initial size of c-PMMA spheres (ca. 300 nm). This shrinkage is caused by the melting of polymer templates and sintering of the produced metal oxides. The wall thicknesses of the catalysts estimated from the SEM images are about 35–45 nm. In addition, the 3DOM structures become less uniform while K^+ ions are introduced. The presence of the low-melting compounds and eutectics may damage the macrostructure of catalysts.

3.1.6. The results of XPS characterization

For catalytic reactions, the surface characteristics are always more important than the bulk ones. Thus, the XPS technique was used to investigate the chemical state and the relative content of the metal elements on the surfaces of $La_{1-x}K_xCoO_3$ catalysts. The La3d peak is a doublet with components at BE of 837.2 and 834.4 eV, as shown in Fig. 5a and Table 2, which is similar to the values recorded from pure lanthana [27]. This indicates that La ions are present in the trivalent form.

Fig. 5b shows the XPS spectra for Co2p of the 3DOM $La_{1-x}K_xCoO_3$ catalysts. Two main peaks corresponding to Co2$p_{3/2}$ and Co2$p_{1/2}$ are detected. The average BE of Co2$p_{3/2}$ in the $LaCoO_3$ catalyst is 779.9 eV, which is close to that reported by Wang et al. [28], and its BE difference between Co2$p_{3/2}$ and Co2$p_{1/2}$ levels is 15.2 eV, indicating that Co^{3+} ions are the dominant valences of Co ions [26]. On the other hand, the BE of Co2$p_{3/2}$ slightly decreases with the increasing K-substituted amount, as listed in Table 2. For $x = 0–0.3$, the Co2$p_{3/2}$ peaks move from 779.9 eV ($x = 0$) to 779.5 eV ($x = 0.3$). These results demonstrate that some amounts of Co^{3+} change into Co^{4+} when La^{3+} ions are partially replaced by K^+ ions, and the content of Co^{4+} increases with increasing K-substituted amounts. A similar phenomenon was reported by Wen et al. [29] that the increase in the Co valence state induces a shift toward the low BE sites. In this case of $La_{1-x}K_xCoO_3$ catalysts, when monovalent K ions are fully dissolved into the perovskite-type structure, an electronic unbalance is generated. As a result, part of the Co^{3+} ions in the B-sites of perovskite-type structures are changed to Co^{4+} ions to preserve the charge neutrality, which induces the shift to lower BE sites. At the same time, with the increase in the K-substituted amounts, the Co2$p_{3/2}$ peaks of catalysts become wider and stronger, which further reveals the presence of the high-valent Co ions.

There are three main chemical states of oxygen in the $La_{1-x}K_xCoO_3$ catalysts, and they can be fitted into three kinds of oxygen species, as shown in Fig. 5c and Table 2. The low BE peaks at 528.5–528.7 eV may be ascribed to the lattice oxygen species (O_{lat}: O^{2-}). The high BE peaks at 531.0–531.3 eV are attributed to the adsorbed oxygen species ($O_{ads}: O_2^{2-}$ or O^-), and the peaks of BE at 533.4 eV are due to the adsorbed molecular water [30]. Many experimental data collected in recent years show that O_2^{2-}/O^-

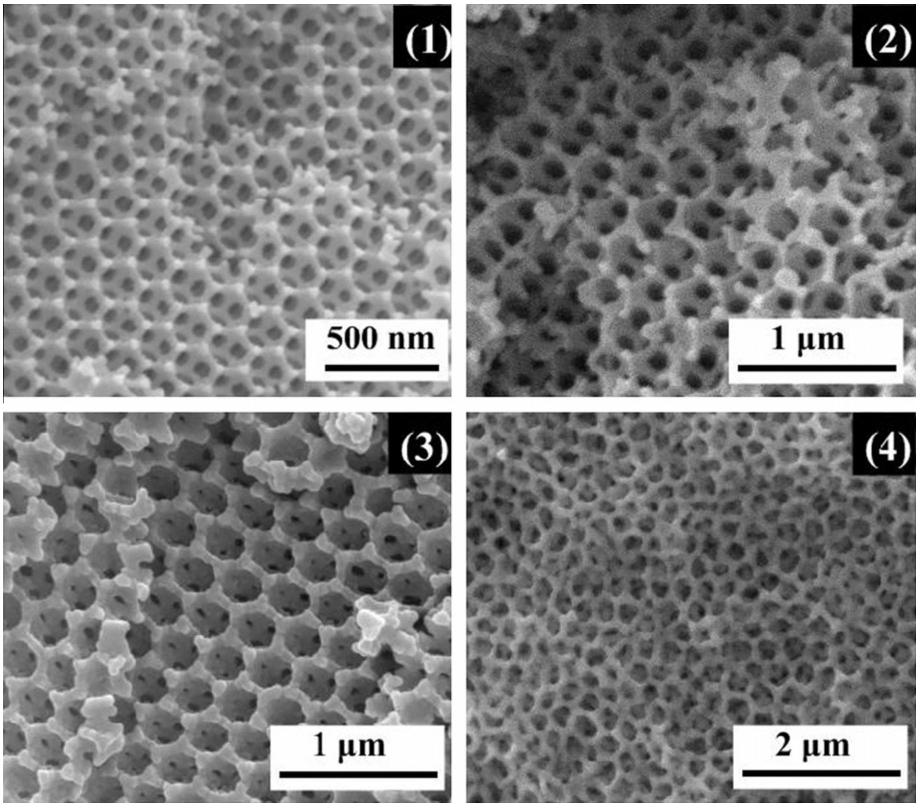

Fig. 4. The SEM images of the 3DOM $La_{1-x}K_xCoO_3$ catalysts: (1) $LaCoO_3$; (2) $La_{0.9}K_{0.1}CoO_3$; (3) $La_{0.8}K_{0.2}CoO_3$; (4) $La_{0.7}K_{0.3}CoO_3$.

species are strongly electrophilic reactants that are very active for oxidation, especially in the low–temperature range. Thus, O_{ads} species are responsible for the total oxidation and the area ratio of O_{ads}/O_{lat} is very important for the oxidative performances [31]. From Table 2, it can be seen that the relative concentrations of oxygen species are different. The O_{ads}/O_{lat} ratios of K-substituted catalysts are greater than that of $LaCoO_3$, and they increase with increasing K-substituted amounts. This result strongly demonstrates that large numbers of oxygen vacancies may be formed when La^{3+} ions are partially replaced by K^+ ions, and the increasing O_{ads} species content leads to an increase in the activity of the catalyst.

3.1.7. The results of H_2-TPR characterization

For metal oxide catalysts, H_2-TPR measurement can simultaneously reflect the reducibility of metallic ions with high valence to ions with low valence or metal atoms, and the potential to remove or take up oxygen, i.e., the mobility of the lattice oxygen [32]. Thus, it reflects the redox ability of the catalyst. In this work, the temperature of the reduction peak (T_{red}) is taken as a measure to evaluate the redox ability of the catalyst. Since the rate of soot oxidation at low temperature is more important than that at high temperature in practical applications, we especially focus on the lowest T_{red} of H_2 TPR. Fig. 6 shows the H_2-TPR profiles of the 3DOM $La_{1-x}K_xCoO_3$ catalysts. The two reduction peaks of 3DOM $LaCoO_3$ indicate that two reduction stages occurred, namely α (430 °C) and β (600 °C). The α peak could be due to the reduction in O_{ads}, as well as to the possible reduction in Co^{3+} to Co^{2+}. The β peak may be assigned to the shift from Co^{2+} to Co^0 and the reduction in O_{lat} [33,34].

In the case of K-substituted catalysts, new reduction peaks are observed at around 350 °C, as shown in Fig. 6. The T_{red} of K-substituted catalysts all shift to lower temperatures compared with that for $LaCoO_3$. This phenomenon may be due to the existence of Co^{4+} ions when La^{3+} ions are partially replaced by K^+ ions. The Co^{4+} can be reduced to Co^{3+} at a relatively low temperature [28]. Furthermore, the areas of the reduction peaks at low temperature become much larger with increasing K-substituted amounts, as shown in Fig. 6 and Table 3. It is mainly due to the increase in the amounts of the Co^{4+} ions and the O_{ads}, which will consume more H_2. As suggested by Zhang et al. [35], the rapid desorption of oxygen at low temperature is related to the relatively easy redox process of $M^{(4-\delta)+} \rightarrow M^{3+}$. The chemical potential and the reactivity of oxygen adjacent to M cations will become higher with the increasing oxidation state and the content of high-valent M cations. This mechanism is consistent with our H_2-TPR results. Therefore, when K^+ ions are introduced into A-sites of the perovskite-type structures to partially replace La^{3+} ions, the redox properties of catalysts are improved remarkably.

3.2. Catalytic activity results

3.2.1. The TPO reaction

Table 4 lists the T_{50} and S^m_{CO2} for soot combustion over catalysts and without catalyst under conditions of loose contact between soot and catalyst. Compared with the T_{50} and S^m_{CO2} of bare soot, which are 585 °C and 55.0%, respectively, all the catalysts examined are active in promoting soot combustion. The 3DOM catalysts show higher catalytic activities (i.e., lower combustion temperature and higher selectivity of CO_2) than the corresponding nanoparticle ones. Compared with nanoparticle catalysts, the T_{50} of corresponding 3DOM catalysts is further lowered by ca. 20 °C and the S^m_{CO2} of 3DOM samples are all greater than 99.5%. Furthermore, the soot combustion temperatures are further lowered over all the 3DOM K-substituted catalysts compared with 3DOM $LaCoO_3$. Among these catalysts, the 3DOM $La_{0.9}K_{0.1}CoO_3$ catalyst gives the highest catalytic activity, and its T_{50} and S^m_{CO2} are 378 °C and 99.8%, respectively. This catalytic activity of T_{50} is as

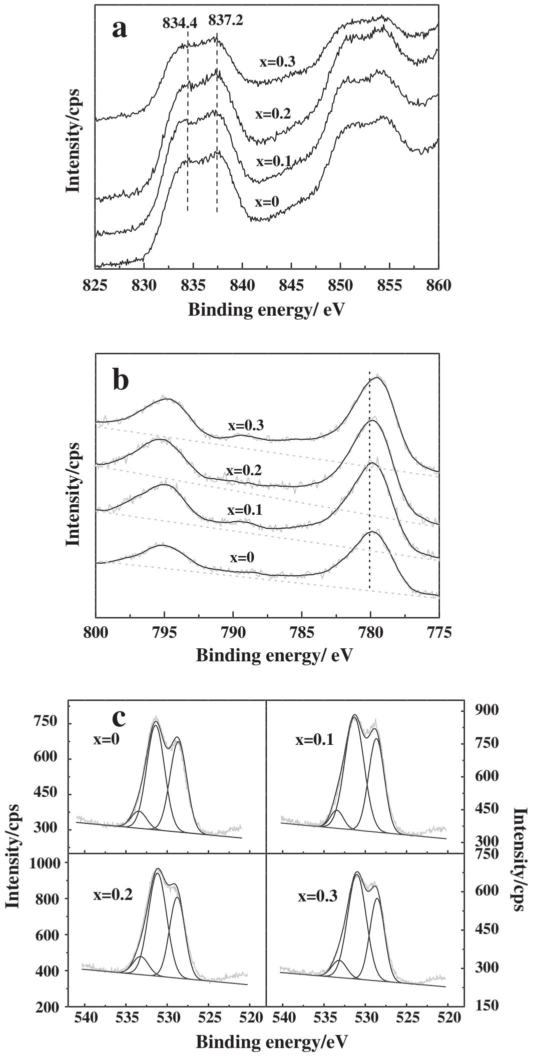

Fig. 5. The XPS spectra for La3*d* (a), Co2*p* (b), and O1*s* (c) of 3DOM $La_{1-x}K_xCoO_3$ catalysts.

good as that of noble metal Pt catalyst, which is the best catalyst system so far reported for soot combustion under conditions of loose contact. In addition, the catalysts could hold the 3DOM perovskite-type structure after the TPO reactions, which could be evidenced by XRD and SEM results (Figs. S6 and S7 in the Supplementary Information).

3.2.2. The isothermal reaction

Fig. 7 shows the CO_2 concentrations at 320 °C as a function of time over 3DOM $La_{1-x}K_xCoO_3$ catalysts before and after the removal of O_2 from the reactant feed. Table 5 lists the quantified values of the reaction rate, the density of active redox sites, and the TOF for soot combustion under O_2 at 320 °C over the 3DOM $La_{1-x}K_xCoO_3$ catalysts. The TOF values ($2.06–2.17 \times 10^{-3}$) of the catalysts are quite large, which indicates that the sites are very active for soot combustion. Moreover, the TOF value slightly increases with the increase in the K-substituted amount, indicating gradual improvement of the redox properties of catalysts. This is in agreement with the H_2 TPR results. In addition, the reaction rates of K-substituted catalysts for soot combustion are greater than that of $LaCoO_3$, as listed in Table 5. These results are consistent with those for the T_{50} of catalysts in the TPO reactions.

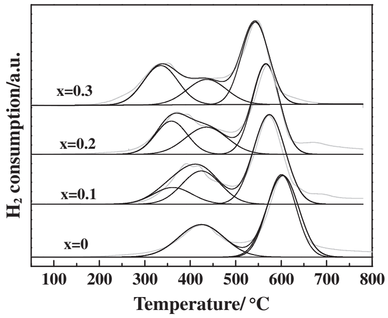

Fig. 6. The H_2-TPR profiles of 3DOM $La_{1-x}K_xCoO_3$ catalysts.

4. Discussion

4.1. The synthesis of 3DOM complex oxide

After one decade of research on CCT methods to produce 3DOM structures, advances in synthetic techniques driven by the demands of potential applications have led to great strides in the structural and compositional complexity of these materials. Most commonly, 3DOM metal oxides are synthesized from monodisperse colloidal crystals [36], typically silica or polymer spheres. Unlike most natural hard templates, such as bioskeletons, viruses, or plant components, this template boasts a high degree of periodicity in three dimensions, which is also translated into a replica of the 3DOM structure [37]. For preparing the 3DOM complex metal oxides, the polymer spheres are superior to silica spheres as templates because of (1) the controllability of the connectivity of the macropores due to the soft characteristics of polymer spheres; (2) the ease of removing the polymer templates; and (3) the multitude of available polymer colloidal sizes and shapes [38]. The polymer templates, which can support the precursor converting to a solid state framework at low temperature, play a key role in the successful synthesis of 3DOM complex metal oxides in the polymer CCT method. The T_g of polymer spheres should be higher than or similar to the T_s of metal nitrates. Only in this way can we

Table 2
XPS results for 3DOM $La_{1-x}K_xCoO_3$ catalysts.

Catalysts	La		Co			O						
			$2p_{1/2}$	$2p_{3/2}$	ΔBE	H_2O		O_{lat}[b]		O_{ads}[c]		O_{ads}/O_{lat}
	BE[a]		BE			BE	Area	BE	Area	BE	Area	
$LaCoO_3$	834.4	837.2	795.1	779.9	15.2	533.4	168	528.6	984	531.3	1199	1.22
$La_{0.9}K_{0.1}CoO_3$	834.2	837.1	795.0	779.8	15.2	533.4	161	528.5	1021	531.2	1509	1.48
$La_{0.8}K_{0.2}CoO_3$	834.5	837.1	795.1	779.8	15.3	533.3	235	528.7	1045	531.3	1581	1.51
$La_{0.7}K_{0.3}CoO_3$	834.5	837.2	795.0	779.5	15.5	533.3	151	528.5	717	531.0	1153	1.61

[a] Binding energy (eV).
[b] The lattice oxygen species.
[c] The adsorbed oxygen species.

Table 3
The temperatures and area ratio of reduction peaks in the H_2 TPR.

Catalysts	Low-temperature stage				High-temperature stage	
	T_{red} (°C)[a]	Area ratio (%)	T_{red} (°C)[a]	Area ratio (%)	T_{red} (°C)[a]	Area ratio (%)
$LaCoO_3$	–	–	424	36.11	604	63.89
$La_{0.9}K_{0.1}CoO_3$	361	14.60	424	26.74	574	58.66
$La_{0.8}K_{0.2}CoO_3$	359	22.57	436	24.37	567	53.06
$La_{0.7}K_{0.3}CoO_3$	335	29.45	436	21.61	543	48.93

[a] The temperature of the reduction peak.

Table 4
The T_{50} and S^m_{CO2} for soot combustion over catalysts and without catalyst (loose contact condition).

Catalysts	T_{50} (°C)[a]		S^m_{CO2} (%)[b]	
	3DOM[c]	Nano[d]	3DOM[c]	Nano[d]
Bare soot	585		55.0	
$LaCoO_3$	406	421	99.5	99.1
$La_{0.9}K_{0.1}CoO_3$	378	398	99.8	98.3
$La_{0.8}K_{0.2}CoO_3$	383	410	99.8	98.4
$La_{0.7}K_{0.3}CoO_3$	380	400	99.5	98.4

[a] The temperatures at which 50% of the soot was oxidized during the TPO procedure.
[b] Selectivity to CO_2 formation at the maximum temperature at which soot-burnt rate was the highest.
[c] The three-dimensionally ordered macroporous samples.
[d] The nanoparticle samples.

solidify the precursor. However, the T_g of the common PMMA spheres is much lower than the T_s (close to 130 °C) of cobalt nitrate, as evidenced by the TG–DSC analysis. When thermally treated above the T_g, the polymer templates melt and the void spaces among the spheres decrease, so that the precursor that has not been completely solidified will be squeezed out of the templates [39]. Thus, the common PMMA spheres cannot meet the requirement for the preparation of 3DOM $La_{1-x}K_xCoO_3$ catalysts. To solve this problem, a surface modification technology for improving the thermal stability of polymer spheres was used in this work. The AA as a functional monomer can offer the carboxyl groups to the surfaces of PMMA spheres. In the right proportions, the copolymerization of MMA and AA could generate large amounts of hydrogen bonds, which can improve the intermolecular forces. Thus, the thermal stability of the copolymer spheres is enhanced and the T_g has been raised to 130 °C, evidenced by the DSC result (Fig. S2 in the Supplementary Information). This T_g is similar to the T_s of cobalt nitrate. Therefore, the nitrate oxides could be successfully converted to solid state metal glyoxylates before the melting of the copolymer templates.

Furthermore, another key point in achieving a satisfactory 3DOM structure is the efficient infiltration of the templates by the precursor solution. However, the viscosities of many metal precursor solutions are too high for them to occupy all the interstitial space among the templates. Thus, the orderly regularity of the macroporous structure is weakened. In order to increase the filling content of the precursor, Villaescusa et al. [40] used the multiple infiltration method via spin coating to obtain a porous silica film. But this method is not suitable for preparing monolithic catalysts because the outer channels are easily blocked after initial infiltration, preventing further diffusion of precursor solution toward the interior voids of templates. The methanol, as a kind of polar diluent, could decrease the viscosity of solution. Thus, diluting the metal nitrate with methanol solution in this work could efficiently decrease the diffusion resistance and increase the penetration rate of precursor. As shown in Fig. S3b in the Supplementary Information, the spaces between close-packed spheres are efficiently filled

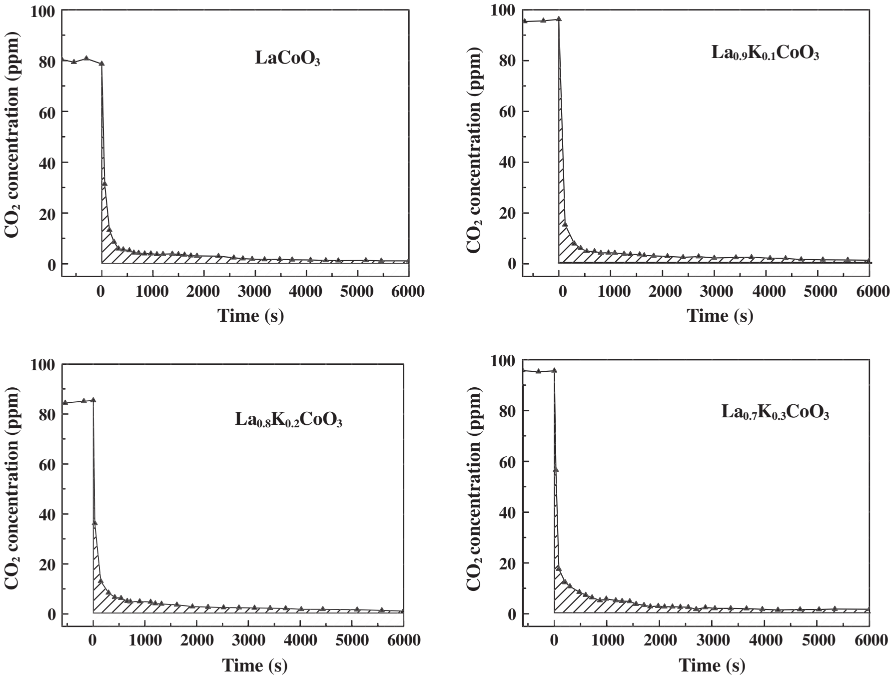

Fig. 7. The CO_2 concentrations as a function of time over 3DOM $La_{1-x}K_xCoO_3$ catalysts before and after O_2 is removed from the reactant feed. Reaction at 320 °C.

Table 5
Reaction rate, active oxygen (O*) density, and TOF values for soot combustion with O_2 at 320 °C over the 3DOM $La_{1-x}K_xCoO_3$ catalysts.

Catalysts	v (mol s^{-1} g^{-1} × 10^{-7})[a]	v^* (mol s^{-1} m^{-2} × 10^{-9})[b]	O* amount (mol g^{-1} × 10^{-5})[c]	O* density (nm^{-2})[d]	TOF (s^{-1} × 10^{-3})[e]
$LaCoO_3$	0.85	2.87	4.14	0.84	2.06
$La_{0.9}K_{0.1}CoO_3$	1.06	3.87	4.99	1.10	2.12
$La_{0.8}K_{0.2}CoO_3$	0.97	4.27	4.53	1.20	2.14
$La_{0.7}K_{0.3}CoO_3$	1.05	5.07	4.86	1.41	2.17

[a] Reaction rate.
[b] The specific reaction rate unit BET surface area.
[c] The number of active redox sites.
[d] The density of active redox sites.
[e] The ratio of the reaction rate to the active site density.

by precursor solution, indicating that the diluted inorganic precursor is able to diffuse easily through the interstitial voids of templates.

Finally, the removal of the templating spheres is also very important for the preparation of a uniform macrostructure. In general, the polymer spheres are removed by calcination, which not only opens up the macropore spaces but also steers the skeleton formation and influences the local architecture of the skeleton. In the calcination process, the heat produced by oxidative decomposition of polymer templates should be sufficiently transferred/removed. Only in this way, we can ensure a uniform macrostructure without collapse. Thus, the inert environment and a low heating rate (1 °C/min) were used in this work to inhibit the drastic melting of the polymer spheres. At the same time, the quartz sand and gases flowing were employed to transfer or remove the heat produced in the calcination process. Slightly heating the polymer templates at the T_g of spheres for a few moments could strengthen the templates and also cause spheres to merge partially. Thus, keeping heat treatment at 130 °C for 2 h under Ar not only further enhances the solidification of the precursor solution to a hard solid state framework, but also enlarges the diameters of interconnecting windows among macropores. However, when the temperature reaches 400 °C, the polymer templates will be completely decomposed and the macroporous framework will collapse if there is no other hard template to support them.

In this work, the calcination process had been optimized; i.e., the samples were first calcined under Ar and then in air. The sp^2-hybridized carbon atoms of c-PMMA spheres could be converted to sturdy amorphous carbon by calcination under Ar. They can act as hard templates to prevent the macroporous structure from collapsing while the polymer templates completely decompose. The detailed calcination process was analyzed by TG–DSC. Fig. 8 shows the TG–DSC curve of the precursor/template mixture under Ar. The weight loss from room temperature to 89 °C with an endothermic DSC peak is ascribed to the evaporation of methanol and H_2O. The evaporation of methanol before the melting of the c-PMMA spheres could make some space in the precursor framework and reduce the amount of precursor that is squeezed out of the voids while the polymer templates melt. This is equivalent to enhancing the thermal stability of templates and is favorable for the transformation of the metal nitrates to a solid state framework. An exothermic peak, which shows a weight loss at ca. 130 °C, is ascribed to the oxidation of ethylene glycol by metal nitrate to the metal glyoxylate ($[C_2H_2O_4]^{2-}$) or oxalate ($[C_2O_4]^{2-}$) and the release of NO_x gas [20]. This indicates that the solidification temperature of the metal nitrates is ca. 130 °C. The weight loss from 230 to 420 °C with an endothermic peak corresponds to the decomposition of c-PMMA spheres, which can be evidenced by the TG analysis of c-PMMA spheres under Ar (Fig. S4 in the Supplementary Information). When the macroporous framework of metal oxides has been completely solidified, the carbon templates can be removed by calcination in air to leave the 3DOM metal oxides [38]. The presence of the carbon templates and their removal in the final products were evidenced by the TG–DSC, Raman, and EDS results (Fig. S4, S5, and Table S1 in the Supplementary Information).

In a word, the 3DOM complex metal oxides can be successfully obtained after the effective synthesis and assembling of c-PMMA templates, the efficient infiltration of precursor solution, the complete solidification of the macroporous framework, and the full removal of templates by calcination.

4.2. The influence of the intrinsic activity of catalyst for soot combustion

Soot combustion is a kind of deep oxidation reaction. The catalytic nature of the reaction is a redox process. Therefore, the redox properties of the catalyst determine its intrinsic activity. The TOF value is defined as the quantified value of the intrinsic activity. Thus, the catalyst that has better redox properties will show higher intrinsic activity and a larger TOF value.

To calculate the TOF value, the reaction rate in the kinetic regime is first determined by the gas analyses with an online gas chromatograph in the isothermal reaction. Because a relatively high feed flow rate (150 ml/min) and low reaction temperature

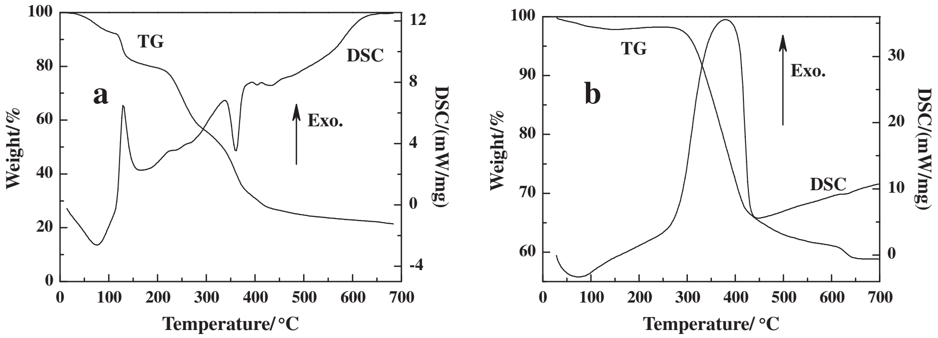

Fig. 8. The TG–DSC curves of (a) the precursor/template mixture under Ar and (b) CMCCT-Ar in air.

(320 °C) are used, the CO_2 signal remains nearly unchanged at a long reaction time, as shown in Fig. 7. Thus, the reaction rate for soot combustion can be obtained according to the concentration of CO_2 per unit time.

More significantly, accurate identification and quantification of the active redox site density are critical for determining TOF values of the catalysts for redox reactions, which is sometimes very difficult for heterogeneous catalysis. Numerous probe methods have been used to quantify the density of active sites available on supported and bulk metal oxide catalysts. For supported catalysts, the metal sites are known to be active and the number can be obtained by H_2 [41] or CO [42] chemisorption. For bulk catalysts, O_2 chemisorption after H_2 prereduction has been used as a redox site probe, which involves reducing the catalyst surface with H_2 and then reoxidizing to determine the number of redox sites by the amount of O_2 adsorbed [43]. However, these methods are not suitable for solid–solid reactions such as soot combustion on metal oxide catalysts, because the actual reactant is not used as the probe molecule, and both the bulk reduction in the oxide during high-temperature chemisorption and physisorbed oxygen during low-temperature chemisorption can lead to incorrect estimates of the number of redox sites. Very recently, isothermal anaerobic titration at the reaction temperature with the actual reactant as the probe molecule has been shown to be an accurate technique for quantifying active redox site densities in metal oxide catalysts, in which all conditions are similar to those of actual reactions except for the presence of oxygen in the gas phase [22,44]. Inspired by these works, we quantified the active oxygen site densities for soot combustion over the 3DOM $La_{1-x}K_xCoO_3$ catalysts in isothermal anaerobic titration by integrating the diminishing rate of CO_2 formation over time after O_2 was removed from the reactant feed. Because the CO_2 is produced from the interaction of the active oxygen and the reactant soot, the active site density of the catalyst is equal to twice the amounts of CO_2 that can be measured from the shaded areas, as shown in Fig. 7 with the online gas chromatograph. Finally, the TOF value could be obtained by calculating the ratio of the reaction rate to the active site densities of catalysts. Since the redox ability of $LaCoO_3$ is the strongest among various perovskite-type oxides and its TOF value ($2.06 \times 10^{-3}\ s^{-1}$) calculated in this work is also quite large, the $LaCoO_3$ catalyst will have excellent intrinsic activity for soot combustion.

Moreover, in order to further enhance the intrinsic activities of catalysts, the effect of K cation substitution into the perovskite-type structure was investigated in this work. For perovskite-type oxide catalyst, B-site cations during soot combustion possess the function of catalysis. The cation at the A-site (La^{3+}) is generally trivalent, as La^{3+} ions at A-sites are partially replaced by K^+ ions. According to the principle of electron neutrality, the positive charge reduced could be balanced either by the formation of a higher oxidation state ion at the B-site [45], i.e.,

$$Co^{3+} \rightarrow Co^{4+}$$

$$La_{1-x}K_xCo^{3+}_{1-2x}Co^{4+}_{2x}O_3 \rightarrow LaCoO_3 + xLa^{3+}|K^+|'' + 2xCo^{3+}|Co^{4+}|^{\bullet},$$

or by the formation of an oxygen vacancy (V_0) in $La_{1-x}K_xCoO_3$,

$$La_{1-x}K_x\lambda(V_0)Co^{3+}O_{3-\lambda} \rightarrow LaCoO_3 + xLa^{3+}|K^+|'' + \lambda|O|^{\bullet\bullet}$$

Therefore, when K^+ is substituted in $LaCoO_3$, the positive charge reduction should be balanced. On one hand, partial low-valence Co ions (Co^{3+}) will change to high valence (Co^{4+}) in $La_{1-x}K_xCoO_3$ catalysts. Co^{4+} ions have a higher oxidizing activity than that of Co^{3+} ions; therefore, it can further lower the temperature for soot combustion. On the other hand, these structural defects and anion vacancies will accelerate the mobility of lattice oxygen and facilitate the reproduction of oxygen vacancy. It can be expected that the rate of active oxygen generation during the reaction is much faster than that of its combination to give gas-phase O_2. The creation of such active oxygen species will lower the temperature of soot oxidation. The XPS results also demonstrate that the amounts of surface-adsorbed oxygen and oxygen vacancy concentration of $La_{1-x}K_xCoO_3$ increase with increasing K-substituted amounts. The presence of a large number of oxygen vacancies will favor the adsorption and activation of molecular oxygen on the catalyst surface. Thus, the K-substituted catalysts have better redox properties than the $LaCoO_3$ catalyst, which leads to higher TOF values, as listed in Table 5. Meanwhile, all the K-substituted catalysts show higher catalytic activity for soot combustion. This indicates that the redox properties of the catalyst determine its intrinsic activity, which is the interior factor influencing catalytic activity. Catalysts that have good redox properties will have high catalytic activity.

However, it is noted that a linear relationship is not observed between the TOF values of the K-substituted catalysts and their catalytic activities (i.e., the soot combustion temperatures) for soot combustion. This suggests that the redox property is not the sole factor affecting the activity of the catalyst, and some other factors such as the contact between soot and catalyst might also play an important role. In conventional catalytic systems, the transport of soot particles to the outer surface-active oxygen of catalysts seems not to be a problem, but the small pore sizes of catalysts make for the transfer of soot particles into the inner pores to touch other active oxygen difficult. This is because most of the active oxygen sites are produced on the internal surfaces of catalysts. Therefore, searching for new catalytic systems to improve the contact between soot and catalyst is an important task. 3DOM catalysts will provide an option to enhance the loose contact activity for soot combustion.

4.3. The relation between the structures of catalysts and their catalytic performance for soot combustion

Soot combustion takes place at the three-phase boundary between a solid catalyst, a solid reactant (soot), and gaseous reactants (O_2, NO). Thus, the efficiency of catalysts is strongly influenced by the contact between soot and catalyst. In many studies, the catalytic performance of catalysts for soot combustion is excellent under tight contact between soot and catalyst. However, there is loose contact between catalysts on the surface of filter and soot particles under practical conditions [46]. Thus, it is important to study and design active catalysts for soot combustion under loose contact conditions. In our previous work, we have reported that supported vanadium oxides and K-promoted vanadium oxides are good candidate catalysts for diesel soot oxidation [47]. Their high activities have been related to their low melting points, which ensure good contact between soot and catalyst. Furthermore, many nanoparticle catalysts also show high catalytic activity for soot combustion, attributed to the good mobility and high intrinsic activity of surface atoms in nanometric particles [11]. However, the catalytic activity of these catalysts is weakened, in that their small pore sizes limit the entry and transport of soot particles into their inner pores. In this work, the pore sizes of the 3DOM catalysts exceed 240 nm, which is much larger than the size of soot particles. Moreover, the periodic voids are well interconnected through open windows and the skeletal structure, whose shape depends on the interactions between precursor and template, is also interconnected. This bicontinuous nature of the structure [37] can serve transport applications through both phases: transport of the soot particles in the macropore phase and of CO and O_2 molecules in the solid phase. These properties are very favorable for the catalytic combustion of soot particles. Thus, the soot particles can easily enter the interior of 3DOM catalysts and have less resistance going through the catalyst structure. The catalyst is in close proximity to soot particles, and more catalyst surface is exposed to reaction atmosphere. This will increase the amount of activated oxygen over the catalysts and decrease the temperature of soot oxidation. As shown in Table 4, all the 3DOM catalysts show lower soot oxidation temperatures, which indicates the obvious advantage of the 3DOM structure for soot combustion. Moreover, the high oxygen mobility improves the selectivity of CO_2. It is possible to produce relatively large amounts of CO during soot combustion because the oxygen amounts in air can be depleted quickly. CO formation would cause an additional environmental problem. However, the highly mobile oxygen existing in the catalysts may offer oxygen for soot oxidation, thus decreasing the CO amount. For example, 3DOM $La_{0.9}K_{0.1}CoO_3$ catalyst produces more mobile oxygen, leading to 99.8% selectivity of CO_2 production at T_{50} compared with 98.3% over nanoparticle catalyst. In addition, the relatively high BET surface area of the catalyst is also due to the uniform structure. The unique 3DOM structure will remarkably enhance the contact between the soot and catalytic active sites, and then substantially improve its catalytic performance for soot combustion. Therefore, based on both good redox property and uniform macroporous structure, $La_{0.9}K_{0.1}CoO_3$ shows the highest catalytic activity for soot combustion.

Based on the results and discussion above, good redox properties and the interconnected uniform macroporous framework can lead to high catalytic activity of 3DOM $La_{1-x}K_xCoO_3$ perovskite-type oxide catalysts for soot combustion. The catalytic oxidation of soot over 3DOM catalysts is shown in the graphical abstract. The soot particles are transferred by the reactant gas flow into the inner pores of catalysts through the interconnected macroporous tunnel. The surface-active oxygen bound to Co^{4+}/Co^{3+} reacts with soot at the soot/catalyst interface to give out CO_x, following the reproduction of oxygen vacancies and the reduction in high-valent Co ions. Thus, the low-valent Co ions may be reoxidized and surface-active oxygen is also reproduced, on which the next combustion of soot takes place. In this redox cycle, the soot particles will be completely combusted over the catalysts. Although this work only demonstrated the use of 3DOM materials for diesel soot combustion, we expect that they could be applied to any other chemical reaction and separation of solid particles with large size. Furthermore, the versatility of the CMCCT method should, in principle, be applicable to prepare other 3DOM complex metal oxides whose preparation is limited by the polymer CCT theory.

5. Conclusions

(1) Three-dimensionally ordered macroporous (3DOM) $La_{1-x}K_xCoO_3$ perovskite-type oxide catalysts with large pore sizes and interconnected macroporous structure were successfully synthesized by the carboxy-modified colloidal crystal template method, which overcomes the limitations of the polymer colloidal crystal template method. In this novel method, carboxy-modified poly(methyl methacrylate) (c-PMMA) spheres with sp^2-hybridized carbon atoms were employed as templates and the impregnation and calcination processes were optimized. After the templates were removed, 3DOM $La_{1-x}K_xCoO_3$ perovskite-type oxide catalysts were obtained. Their pore sizes were about 240–260 nm, and the wall thicknesses were about 35–45 nm.

(2) The whole preparation process of 3DOM $La_{1-x}K_xCoO_3$ perovskite-type oxide catalysts was analyzed in detail in situ by means of TG–DSC. The T_g of the c-PMMA spheres could increase to ca. 130 °C. Thus, the metal nitrate could be solidified to a solid state framework using the c-PMMA spheres as soft templates. Moreover, when the c-PMMA spheres were calcined under Ar, the sp^2-hybridized carbon atoms could be converted to a sturdy amorphous material that could be used as a hard template to prevent the macrostructure of catalysts from collapsing. The soft and hard templates were the two key points for obtaining the 3DOM $La_{1-x}K_xCoO_3$ perovskite-type oxide catalysts.

(3) The 3DOM $La_{1-x}K_xCoO_3$ perovskite-type oxide catalysts, which combine excellent redox properties and good contact between soot and catalyst, exhibited supercatalytic performance for soot oxidation. The T_{50} of all 3DOM catalysts was lower than that of corresponding nanoparticle catalysts, and they had the relatively high turnover frequency values. Moreover, all the K-substituted catalysts, which have superior redox properties, showed higher catalytic activities than $LaCoO_3$. Among the studied catalysts, the 3DOM $La_{0.9}K_{0.1}CoO_3$ catalyst had the highest catalytic activity and its soot oxidation temperature, at which 50% of the soot was oxidized (T_{50}), and the selectivity of CO_2 production at T_{50} were 378 °C and 99.8%. The T_{50} of 3DOM $La_{0.9}K_{0.1}CoO_3$ was as good as that of noble metal Pt catalyst, which was the best catalyst system so far reported for soot combustion under loose contact conditions.

Acknowledgments

This work was supported by the National Natural Science Foundation of China (Nos. 20833011, 20803093, and 21073235), the 863 Program of China (No. 2009AA06Z313), the NCET-10-0811 the Doctor Select Foundation (No. 200804251016), and the CNPC Innovation Fund (2010D-5006-0402).

Appendix A. Supplementary material

Supplementary data associated with this article can be found, in the online version, at doi:10.1016/j.jcat.2011.03.024.

References

[1] Z.P. Liu, S.J. Jenkins, D.A. King, J. Am. Chem. Soc. 126 (2004) 10746.
[2] M.V. Twigg, Appl. Catal. B 70 (2007) 2.
[3] D. Reichert, T. Finke, N. Atanassova, H. Bockhorn, S. Kureti, Appl. Catal. B 84 (2008) 803.
[4] J. Liu, Z. Zhao, C.M. Xu, A.J. Duan, G.Y. Jiang, J. Phys. Chem. C 112 (2008) 5930.
[5] L. Castoldi, R. Matarrese, L. Lietti, P. Forzatti, Appl. Catal. B 90 (2009) 278.
[6] W.F. Shangguan, Y. Teraoka, S. Kagawa, Appl. Catal. B 16 (1998) 149.
[7] J. Liu, Z. Zhao, C.M. Xu, A.J. Duan, Appl. Catal. B 78 (2008) 61.
[8] J.L. Hueso, A. Caballero, M. Ocaña, A.R. González-Elipe, J. Catal. 257 (2008) 334.
[9] J. Liu, Z. Zhao, J. Wang, C.M. Xu, A.J. Duan, G.Y. Jiang, Q. Yang, Appl. Catal. B 84 (2008) 185.
[10] S.B. Simonsen, S. Dahl, E. Johnson, S. Helveg, J. Catal. 255 (2008) 1.
[11] J. Liu, Z. Zhao, J. Lan, C. Xu, A. Duan, G. Jiang, X. Wang, H. He, J. Phys. Chem. C 113 (2009) 17114.
[12] B.R. Stanmore, J.F. Brilhac, P. Gilot, Carbon 39 (2001) 2247.
[13] M. Sadakane, T. Asanuma, J. Kubo, W. Ueda, Chem. Mater. 17 (2005) 3546.
[14] G.Z. Zhang, Z. Zhao, J. Liu, G.Y. Jiang, A.J. Duan, J.X. Zheng, S.L. Chen, R.X. Zhou, Chem. Commun. 46 (2010) 457.
[15] J.F. Xu, J. Liu, Z. Zhao, J.X. Zheng, G.Z. Zhang, A.J. Duan, G.Y. Jiang, Catal. Today 153 (2010) 136.
[16] J.I.L. Chen, G. von Freymann, V. Kitaev, G.A. Ozin, J. Am. Chem. Soc. 129 (2007) 1196.
[17] B.T. Holland, C.F. Blanford, A. Stein, Science 281 (1998) 538.
[18] H. Yan, C.F. Blanford, B.T. Holland, W.H. Smyrl, A. Stein, Chem. Mater. 12 (2000) 1134.
[19] S.S. Hong, G.D. Lee, Catal. Today 63 (2000) 397.
[20] M. Sadakane, T. Horiuchi, N. Kato, C. Takahashi, W. Ueda, Chem. Mater. 19 (2007) 5779.
[21] H. Wang, Z. Zhao, P. Liang, C.M. Xu, A.J. Duan, G.Y. Jiang, J. Xu, J. Liu, Catal. Lett. 124 (2008) 91.
[22] Z.L. Zhang, D. Han, S.J. Wei, Y.X. Zhang, J. Catal. 276 (2010) 16.
[23] Z.L. Zhang, Y.X. Zhang, Z.P. Wang, X.Y. Gao, J. Catal. 271 (2010) 12.
[24] P. Darcy, P. Da Costa, H. Mellottée, J. Trichard, G. Djéga-Mariadassou, Catal. Today 119 (2007) 252.
[25] M. Couzi, P.V. Huong, Anal. Chem. 9 (1974) 19.
[26] N.A. Merino, B.P. Barbero, P. Grange, L.U. Cadus, J. Catal. 231 (2005) 232.

[27] C.K. Jorgensen, H. Berthou, Chem. Phys. Lett. 13 (1972) 186.
[28] Y.G. Wang, J.W. Ren, Y.Q. Wang, F.Y. Zhang, X.H. Liu, Y. Guo, G.Z. Lu, J. Phys. Chem. C 112 (2008) 15293.
[29] Y. Wen, C. Zhang, H. He, Y. Yu, Y. Teraoka, Catal. Today 126 (2007) 400.
[30] L.G. Tejuca, J.L.G. Fierro, J.M.D. Tascon, Adv. Catal. 36 (1989) 237.
[31] P. Tsiakaras, C. Athanasiou, G. Marnellos, M. Stoukides, J.E. ten Elshof, H.J.M. Bouwmeester, Appl. Catal. A 169 (1998) 249.
[32] Z. Zhao, Y. Yamada, A. Ueda, H. Sakurai, T. Kobayashi, Catal. Today 93–95 (2004) 163.
[33] R.M. Navarro, M.C. Alvarez-Galvan, J.A. Villoria, I.D. González-Jiménez, F. Rosa, J.L.G. Fierro, Appl. Catal. B 73 (2007) 247.
[34] S. Irusta, M.P. Pina, M. Menendez, J. Santamaria, J. Catal. 179 (1998) 400.
[35] H.M. Zhang, Y. Shimizu, Y. Teraoka, N. Miura, N. Yamazoe, J. Catal. 121 (1990) 432.
[36] J.E.G.J. Wijnhoven, W.L. Vos, Science 281 (1998) 802.
[37] A. Stein, F. Li, N.R. Denny, Chem. Mater. 20 (2008) 649.
[38] M.C. Orilall, N.M. Abrams, J. Lee, F.J. DiSalvo, U. Wiesner, J. Am. Chem. Soc. 130 (2008) 8882.
[39] T. Sen, G.J.T. Tiddy, J.L. Casci, N.W. Anderson, Chem. Mater. 16 (2004) 2044.
[40] L.A. Villaescusa, A. Mihi, I. Rodriguez, A.E. Garcia-Bennett, H. Miguez, J. Phys. Chem. B 109 (2005) 19643.
[41] S.E. Siporin, R.J. Davis, J. Catal. 225 (2004) 359.
[42] M. Kuriyama, H. Tanaka, S. Ito, T. Kubota, T. Miyao, S. Naito, K. Tomishige, K. Kunimori, J. Catal. 252 (2007) 39.
[43] C.D. Baertsch, S.L. Soled, E. Iglesia, J. Phys. Chem. B 105 (2001) 1320.
[44] H. Nair, C.D. Baertsch, J. Catal. 258 (2008) 1.
[45] R.M.G. Cruz, H. Falcon, M.A. Pena, J.L.G. Fierro, Appl. Catal. B 33 (2001) 45.
[46] J. Oi-Uchisawa, A. Obuchi, S.D. Wang, T. Nanba, A. Ohi, Appl. Catal. B 43 (2003) 117.
[47] J. Liu, Z. Zhao, C.M. Xu, A.J. Duan, L. Zhu, X.Z. Wang, Catal. Today 118 (2006) 315.